




## Article

# Structure-Sensitivity of CO<sub>2</sub> Methanation over Nanostructured Ni Supported on CeO<sub>2</sub> Nanorods

Eleonora Marconi <sup>1</sup>, Simonetta Tuti <sup>1,\*</sup> and Igor Luisetto <sup>2,\*</sup>

<sup>1</sup> Department of Science, “Roma Tre” University, Via della Vasca Navale 79, 00146 Roma, Italy; eleonora.marconi@uniroma3.it

<sup>2</sup> Department of Energy Technologies, Italian National Agency for New Technologies, Energy and Sustainable Economic Development (ENEA), Via Anguillarese 301, 00123 Rome, Italy

\* Correspondence: simonetta.tuti@uniroma3.it (S.T.); igor.luisetto@enea.it (I.L.)

Received: 28 March 2019; Accepted: 18 April 2019; Published: 22 April 2019



**Abstract:** Ni-based oxides are widely investigated as catalysts for CO<sub>2</sub> methanation due to their high activity, high selectivity and low cost. The catalytic performances of Ni-based catalysts depend on support properties that strongly influence the dispersion of the catalytic active phase and the Ni–support interaction. Although the CO<sub>2</sub> methanation is widely studied, the structure sensitivity of methanation on nickel is not completely assessed. Ni/CeO<sub>2</sub> nanorods with different nickel/ceria molar ratios (0.05, 0.10, 0.20, 0.30) were prepared by one-pot hydrothermal synthesis. The effect of nickel content and metal particle size on catalytic activity and selectivity for CO<sub>2</sub> methanation were studied using CO<sub>2</sub>:H<sub>2</sub> = 1:4 stoichiometric ratio at high space velocity (300 L g<sup>−1</sup> h<sup>−1</sup>). Sample structure and morphology were studied by X-ray diffraction (XRD), Brunauer–Emmet–Teller (BET) analysis, field-emission scanning electron microscopy/energy-dispersive spectroscopy (FE-SEM/EDS), H<sub>2</sub>-temperature programmed reduction (TPR), H<sub>2</sub>-temperature-programmed desorption (TPD). Both the CO production and the turnover frequency appear depending on nickel particle size, suggesting a structure sensitivity of the CO<sub>2</sub> methanation on nickel supported on ceria.

**Keywords:** CO<sub>2</sub> methanation; CO<sub>2</sub> valorization; Ni supported on ceria; structure-activity relationship

## 1. Introduction

Carbon dioxide is produced and released in industrial processes, energy production, biomass combustion and gasification, cement kilns and oil refinery. Reducing the CO<sub>2</sub> emissions by prevention, storage [1] or recycling [2,3], is highly desirable to limit the greenhouse effects of high CO<sub>2</sub> concentration in the atmosphere. In particular, the hydrogenation of CO<sub>2</sub> into chemicals or fuels like methane, methanol, dimethyl ether [4–6], or the reduction into syn-gas (CO and H<sub>2</sub>) by dry reforming with methane (DRM) [7–10] are interesting research fields of CO<sub>2</sub> utilization. In the power-to-gas process (PtG) the intermittent excess of electricity, produced by renewable power sources like solar or wind, highly dependent on daytime, season and weather, is utilized to decompose water into hydrogen and oxygen by electrolysis [11,12]. The produced H<sub>2</sub> can be directly used as an energy carrier or it can be reacted with CO<sub>2</sub> to produce methane by the Sabatier reaction (4H<sub>2</sub> + CO<sub>2</sub> → CH<sub>4</sub> + 2H<sub>2</sub>O). Methane is an important energy carrier with existing distribution infrastructure. The synthetic methane contributes to the reduction of greenhouse gas emissions, replacing the natural fossil methane. The CO<sub>2</sub> methanation is an exothermic and thermodynamically favored reaction (ΔH<sup>0</sup> = −164 kJ/mol ΔG<sup>0</sup> = −131 kJ/mol) but kinetically limited, being an 8-electron process occurring above 200 °C in the presence of catalysts. Generally, methanation is studied in the temperature range 200–500 °C, to limit the reverse water gas shift reaction (RWGS: CO<sub>2</sub> + H<sub>2</sub> → CO + H<sub>2</sub>O) producing CO at higher temperatures. Many catalysts, based on different noble or transition metals (Ru, Rh, Ir, Pd, Ni, Fe, Co) supported

on oxides ( $\alpha$ -Al<sub>2</sub>O<sub>3</sub>,  $\gamma$ -Al<sub>2</sub>O<sub>3</sub>, TiO<sub>2</sub>, SiO<sub>2</sub>, ZrO<sub>2</sub>, CeO<sub>2</sub>) or mixed oxides (CeO<sub>2</sub>-Al<sub>2</sub>O<sub>3</sub>, SiO<sub>2</sub>-Al<sub>2</sub>O<sub>3</sub>, MgAl<sub>2</sub>O<sub>4</sub>, CeO<sub>2</sub>-ZrO<sub>2</sub>, Y<sub>2</sub>O<sub>3</sub>-ZrO<sub>2</sub>) show good catalytic performances for CO<sub>2</sub> methanation, and have been investigated in the recent years [12–15]. Among these, Ni-based catalysts are the most extensively investigated materials due to their high activity, high selectivity and low cost. The main drawback of Ni-based catalysts is the carbon deposition due to the Boudouard reaction ( $2\text{CO} \rightarrow \text{C} + \text{CO}_2$ ), carbon dioxide reduction ( $\text{CO}_2 + 2\text{H}_2 \rightarrow \text{C} + 2\text{H}_2\text{O}$ ) and carbon monoxide reduction ( $\text{CO} + \text{H}_2 \rightarrow \text{C} + \text{H}_2\text{O}$ ). The catalytic performances of Ni catalysts depend on support properties that strongly influence the dispersion, the reducibility and the support interaction of nickel.

CeO<sub>2</sub> is one of the most studied catalyst carriers in many catalytic oxidation reactions, due to its ability to store and release oxygen by Ce<sup>3+</sup>/Ce<sup>4+</sup> sites on the surface. In CO<sub>2</sub> methanation, the redox properties of CeO<sub>2</sub> are considered to influence both carbon dioxide and hydrogen activation, and the catalyst's basicity is considered to play a key role in the mechanism [16,17]. Ni-based CeO<sub>2</sub> and Ce-Zr binary oxides exhibit excellent catalytic activity and stability attributed to the redox properties and to the ability to highly disperse nickel [17]. CeO<sub>2</sub> can be prepared in different morphologies: nano-rod ceria (r-CeO<sub>2</sub>), nano-cubic ceria (c-CeO<sub>2</sub>) or nano-octaedral ceria (o-CeO<sub>2</sub>), that may have an effect on the catalytic performances [18]. Ni/r-CeO<sub>2</sub> showed higher activity and coke resistance compared with other morphologies in the dry reforming of methane [19] or methanol [20].

Metal particle size is frequently discussed in the literature as a feature determining the CO/CH<sub>4</sub> selectivity of CO<sub>2</sub> methanation [5,21–23]. Small nanoparticles have been reported to promote CO formation instead of CH<sub>4</sub>. This should be due to different reaction pathways for CO<sub>2</sub> methanation depending on the metal particle size. On both small and large Ni nanoparticles, the co-adsorbed CO<sub>2</sub> and H<sub>2</sub> reagents, form monodentate m-HCOO<sup>−</sup> as a key intermediate. On small metal particles, m-HCOO<sup>−</sup> intermediate is decomposed to CO that, following a consecutive reaction pathway, may be further hydrogenated to CH<sub>4</sub>. Whereas, on large metal particles m-HCOO<sup>−</sup> intermediate may be directly hydrogenated to CH<sub>4</sub>, due to the large H<sub>2</sub> surface coverage, causing a higher CH<sub>4</sub> production rate rather than CO production rate [21–23].

Recently, it has been reported by Beierlein et al. [24] that the CO<sub>2</sub> methanation on highly loaded (14–88 wt%) Ni/Al<sub>2</sub>O<sub>3</sub> catalysts is a structure-insensitive reaction and that the terrace atoms are the active sites, whereas parameters such as metal–support interaction or metal–support interface, do not have a significant influence on the activity. However, in our previous studies, for more diluted (5–12 wt%) Ni/YSZ catalysts, we found a dependence of the activity for methanation on nickel particle size (structure sensitivity): smaller Ni<sup>0</sup> particles were more active for CO formation instead of CH<sub>4</sub> formation [5], and had anti-coking properties [6].

As the structure sensitivity of the methanation reaction over nickel has not been completely assessed in the published literature, a series of Ni/nanorod-CeO<sub>2</sub> catalysts with different Ni loading (2–13 wt%) and different Ni particle size, were studied in order to deepen the structure-sensitivity of methanation on nickel. Samples were characterized by X-ray diffraction (XRD), Brunauer–Emmet–Teller (BET) analysis, field-emission scanning electron microscopy/energy-dispersive spectroscopy (FE-SEM/EDS), H<sub>2</sub>-temperature programmed reduction (TPD) and H<sub>2</sub>-temperature-programmed desorption (TPR) analysis.

## 2. Results

### 2.1. Catalysts' Synthesis

Ni/CeO<sub>2</sub> nanorods (r-CeO<sub>2</sub>) catalysts, containing different nickel nominal molar ratio,  $i = \text{Ni}/\text{Ce}$  ( $i = 0.05$ ,  $i = 0.10$ ,  $i = 0.20$ ,  $i = 0.30$ ), were prepared by hydrothermal one-pot synthesis as described in detail in Section 4.1. Synthesized catalysts were named for short Ni<sub>x</sub>Ce, where  $x = i \times 100$ . The chemical composition (%) was analyzed by energy-dispersive spectroscopy (EDS) and reported in Table 1.

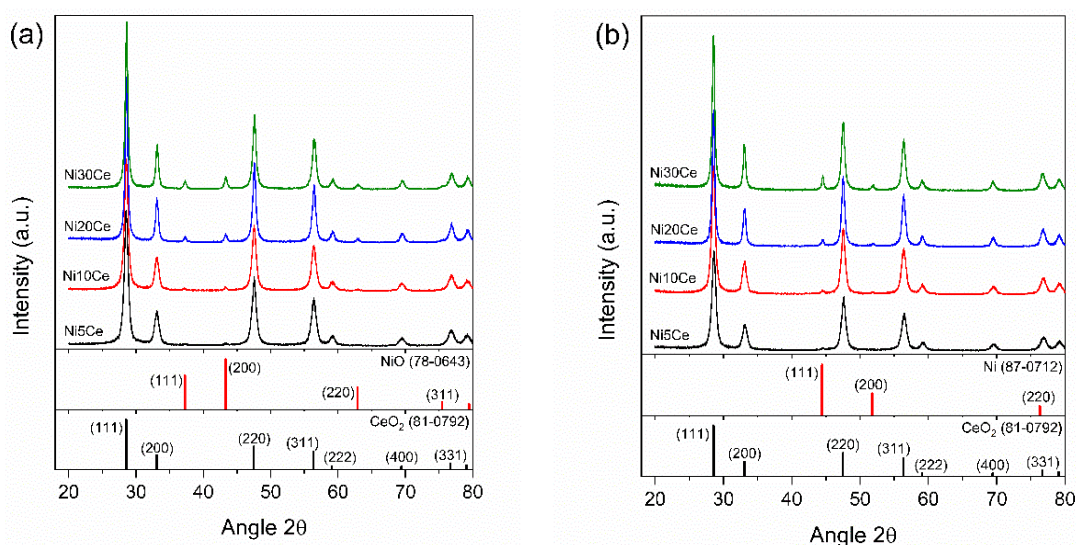
**Table 1.** Chemical composition, textural properties and crystallite size of catalysts.

	Chemical Composition <sup>EDAX</sup> (wt%)		S.A. (m <sup>2</sup> g <sup>−1</sup> )	S.A. <sup>norm</sup> (m <sup>2</sup> g <sup>−1</sup> )	Pore Volume (cm <sup>3</sup> g <sup>−1</sup> )	Pore Size (nm)	d <sub>CeO<sub>2</sub></sub> <sup>XRD</sup> (nm)	d <sub>NiO</sub> <sup>XRD</sup> (nm)	d <sub>Ni</sub> <sup>XRD1</sup> (nm)
	Ni	Ce							
Ni5Ce	1.69	84.31	73	74	0.49	32	11.9	13.6	14.9
Ni10Ce	5.38	83.12	65	69	0.68	39	12.8	21.0	19.0
Ni20Ce	8.46	81.64	34	37	0.28	32	20.2	19.7	21.0
Ni30Ce	13.38	73.90	28	32	0.21	30	18.1	18.1	27.3

<sup>1</sup> on reduced samples.

## 2.2. X-ray Diffraction (XRD) Characterization of Calcined Samples

The X-ray diffractograms of Ni/r-CeO<sub>2</sub> catalysts calcined at 500 °C, together with the CeO<sub>2</sub> and NiO reference JCPDS (Joint Committee on Powder Diffraction Standards) cards, are shown in Figure 1a. All catalysts showed the main reflections at  $2\theta = 28.6^\circ$  (111),  $33.1^\circ$  (200),  $47.6^\circ$  (220),  $56.4^\circ$  (311) typical of CeO<sub>2</sub> fluorite cubic phase (JCPDS card 81-0792) and weak diffraction peaks at  $2\theta = 37.3^\circ$  (111),  $43.5^\circ$  (200),  $62.0^\circ$  (222) assigned to NiO cubic phase (JCPDS card 78-0643). The NiO peaks intensity increased with the Ni content. There are not evidences of CeO<sub>2</sub> reflections shift toward higher  $2\theta$  values, suggesting that the possible incorporation of Ni<sup>2+</sup> ion on CeO<sub>2</sub> lattice, forming a Ni<sub>x</sub>Ce<sub>1-x</sub>O<sub>2-δ</sub> solid solution, is very limited. The mean crystallite size of CeO<sub>2</sub>, d<sub>CeO<sub>2</sub></sub><sup>XRD</sup>, determined from the (111) crystallographic plane by the Debye–Scherrer equation, increased with the nickel loading from about 12 nm up to 18–20 nm (Table 1). The average NiO crystallite size, d<sub>NiO</sub><sup>XRD</sup>, calculated from the (200) reflection, increased from 13.6 nm for Ni5Ce up to 18–21 nm for Ni10Ce, Ni20Ce and Ni30Ce samples (Table 1).

**Figure 1.** X-ray diffraction (XRD) patterns of Ni<sub>x</sub>Ce catalysts: (a) calcined; (b) reduced at 500 °C.

## 2.3. Temperature-Programmed Reduction (TPR) and H<sub>2</sub> Chemisorption

As is well known from the literature, H<sub>2</sub>-TPR profile of CeO<sub>2</sub> shows reduction peaks in the 400–600 °C temperature range, due to the removal of labile oxygen from CeO<sub>2</sub> on the surface, and in the 600–900 °C temperature range, due to reduction of bulk ceria [7,10]. The reduction of NiO supported on CeO<sub>2</sub> generally occurs in the temperature range 400–700 °C, depending on the nickel particle size and on the strength of the nickel-support interactions [7,10]. Temperature-programmed reduction of pure r-CeO<sub>2</sub> and Ni<sub>x</sub>Ce catalysts were performed up to 500 °C (Figure 2a). On pure r-CeO<sub>2</sub>, the surface reduction Ce<sup>4+</sup> → Ce<sup>3+</sup>, with formation of CeO<sub>2-δ</sub>, started above 300 °C, increased up to 500 °C and corresponded to a reduction of about 20% of Ce<sup>4+</sup>. H<sub>2</sub>-TPR profiles of Ni<sub>x</sub>Ce samples showed reduction

peaks in two temperature regions: above 350 °C and below 350 °C. Peaks below 350 °C, less intense, are assigned to the reduction of small NiO particles, or to a very small fraction of  $\text{Ni}^{2+}$  in solid solution with  $\text{CeO}_2$ , Ni–O–Ce. This peak was not observed on the pure  $\text{CeO}_2$  support suggesting that it is related to the presence of nickel, which may facilitate the surface reduction of  $\text{CeO}_2$  according to the reactions (1) and (2) [25,26]. The peak at 380 °C, more intense, is assigned to the reduction of NiO particles highly dispersed on ceria, the weak shoulder above 400 °C is assigned to a small fraction of NiO having a strong Ni–support interaction [27].

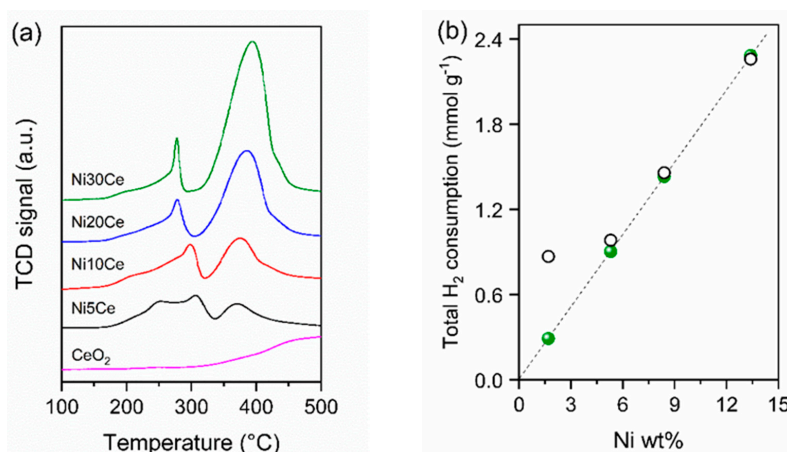


**Figure 2.**  $\text{H}_2$ -temperature-programmed reduction (TPR) analysis: (a) profiles of pure r- $\text{CeO}_2$  and  $\text{Ni}_x\text{Ce}$  catalysts; (b) theoretical (●) and experimental (○) total  $\text{H}_2$  consumption as a function of Ni wt%. The Ni wt% of samples are reported in Table 1.

The total hydrogen consumption in the  $\text{H}_2$ -TPR experiment up to 500 °C, maintaining the final temperature for 1 h, increased with nickel content (Table 2). If all nickel loaded on calcined sample was  $\text{Ni}^{2+}$  and if it was completely reduced below 500 °C, as suggested by the shape and the position of nickel peaks on  $\text{H}_2$ -TPR profiles, the theoretical hydrogen consumption for Ni reduction should correspond to the molar ratio  $\text{H}_2/\text{Ni} = 1$ . The difference between the total experimental and the total theoretical hydrogen consumption is due to the reduction of cerium  $2\text{Ce}^{4+} + \text{H}_2 \rightarrow 2\text{Ce}^{3+}$  and allows evaluating the percentage of  $\text{CeO}_2$  reduced to  $\text{Ce}^{3+}$ . The  $\text{H}_2$  consumption for  $\text{Ce}^{4+}$  reduction and the  $\text{Ce}^{3+}$  percentage are reported in Table 2. The experimental hydrogen consumption was much larger than 1 only for the most diluted samples Ni5Ce, corresponding to a reduction of 20% of ceria, whereas it was very close to 1 for the sample with greater Ni loading, corresponding to a maximum of 2.9% of ceria reduction. According with the literature, the reduction of  $\text{CeO}_2$  in the examined temperatures range depends on the textural properties of the samples, with a linear correlation between surface area and  $\text{H}_2$  consumption [28]. On the sample containing less Ni, with a high surface area, the contribution to the  $\text{H}_2$  consumption, due to the reduction of  $\text{CeO}_2$ -surface, was significant. Whereas on the other samples, the  $\text{H}_2$  consumption due to the reduction of  $\text{CeO}_2$ -surface, became negligible due to the surface area decrement. The total theoretical and experimental  $\text{H}_2/\text{Ni}$  ratio are compared in Figure 2b.

Reduced samples were cooled in hydrogen down to room temperature and the chemisorbed hydrogen was quantified in the subsequent  $\text{H}_2$ -TPD experiment. An evaluation of the size of active nickel particles,  $d_{\text{Ni}}^{\text{TPD}}$ , and of the percentage of nickel dispersion,  $D_{\text{Ni}}$ , was obtained assuming as chemisorption stoichiometry  $\text{Ni}:\text{H} = 1:1$  and are reported in Table 2. As expected, the nickel particle size, increased with nickel content from 3.2 up to 46.8 nm. In agreement with the increase of particle diameter, the corresponding nickel dispersion decreased from 32.0% down to 2.2%.

**Table 2.** Cerium reducibility and nickel dispersion.

Sample	Ni mmol/g	Ce mmol/g	Total H <sub>2</sub> Consumption <sup>1</sup> mmol/g	H <sub>2</sub> /Ni <sup>2</sup> mmol/mmol	H <sub>2</sub> Consumption for Ce <sup>4+</sup> Reduction <sup>3</sup> (mmol g <sup>-1</sup> )	Ce <sup>3+</sup> <sup>4</sup> (%)	d <sub>Ni</sub> <sup>TPD</sup> (nm)	D <sub>Ni</sub> (%)
Ni5Ce	0.29	5.71	0.87	3.00	0.58	20	3.2	32.0
Ni10Ce	0.92	5.54	0.98	1.06	0.08	2.9	12.0	8.5
Ni20Ce	1.44	5.24	1.46	1.02	0.02	1.0	44.2	2.3
Ni30Ce	2.28	4.90	2.26	1.00	0.0	0.0	46.8	2.2

<sup>1</sup> Experimental total H<sub>2</sub> consumption up to 500 °C. <sup>2</sup> Experimental ratio: (total H<sub>2</sub> mol)/(Ni mol). <sup>3</sup> H<sub>2</sub> consumed in Ce<sup>4+</sup> reduction, calculated as: total H<sub>2</sub> for nickel reduction minus theoretical H<sub>2</sub> for nickel reduction: Ni<sup>2+</sup> + H<sub>2</sub> → Ni<sup>0</sup> + 2H<sup>+</sup>. <sup>4</sup> Ce<sup>4+</sup> reduced to Ce<sup>3+</sup> (as percentage): 2Ce<sup>4+</sup> + H<sub>2</sub> → 2Ce<sup>3+</sup> + 2H<sup>+</sup>.

## 2.4. Characterization of Reduced Samples

### 2.4.1. XRD Characterization

The X-ray diffractograms of the Ni/rCeO<sub>2-x</sub> samples, after reduction in H<sub>2</sub> up to 500 °C, (Figure 1b) showed: (i) peaks of fluorite cubic CeO<sub>2</sub>, with the same position, intensity, and full width at half maximum (FWHM), showed by the calcined samples, indicating high sintering resistance of the r-ceria support; (ii) two weak diffraction peaks at  $2\theta = 44.5^\circ$  and  $51.8^\circ$  assigned to (111) and (200) crystallographic plane of the face-centered cubic Ni<sup>0</sup> phase (JCPDS 04-850); (iii) the absence of the NiO phase, indicating that NiO was completely reduced to metallic Ni<sup>0</sup> during the catalytic pre-treatment at 500 °C for 1 h. Ni<sup>0</sup> peaks intensity increased with the Ni content. The average Ni<sup>0</sup> crystallite size,  $d_{\text{Ni}}^{\text{XRD}}$ , on reduced samples with  $x = 5, 10, -20$ , is very close to the dimension of NiO crystallite before sample reduction,  $d_{\text{NiO}}^{\text{XRD}}$ , with no evidence of sintering (Table 1), suggesting a strong interaction of nickel with the ceria support. Only for the most concentrated sample, with a Ni/Ce molar ratio of 0.30, the nickel crystallite size increased from 18 nm for NiO on calcined sample, up to 27.3 nm for Ni<sup>0</sup> after reduction, evidencing a restrained sintering and suggesting a weaker Ni-support interaction.

### 2.4.2. Brunauer–Emmet–Teller (BET) Characterization

The textural properties of the reduced samples are reported in Table 1. NixCe catalysts showed a physisorption isotherm classified as Type II (Figure 3a), typical of non-porous or macroporous material [29]. The N<sub>2</sub> adsorption–desorption curves showed a hysteresis loop of H1 type, with the two branches almost vertical and nearly parallel, characteristic of uniform agglomerates and narrow distributions of pore size [29]. The specific surface area of hydrothermal synthesized pure r-ceria was 90 m<sup>2</sup> g<sup>-1</sup>. The specific area S.A. of NixCe catalysts markedly decreased as a function of Ni content from 73 m<sup>2</sup> g<sup>-1</sup> for Ni5Ce to 28 m<sup>2</sup> g<sup>-1</sup> for Ni30Ce, in agreement with the decrease of the pore volume from 0.49 to 0.21 cm<sup>3</sup> g<sup>-1</sup>. The specific area normalized by subtracting the mass of supported nickel, (S.A.)<sup>norm</sup>, also decreased, from 74 m<sup>2</sup> g<sup>-1</sup> for Ni5Ce to 32 m<sup>2</sup> g<sup>-1</sup> for Ni30Ce, confirming that nickel loading caused the blocking of the pores. By contrast, the pore diameter of samples was in range 30–39 nm and appeared not depending on nickel content, suggesting that the one-pot synthesis did not influence the ceria porosity much (Table 1). The pore size distribution (PSD) profiles of NixCe samples, reported in Figure 3b, showed a similar bimodal pore distribution, with a fraction of pores with diameter 3–6 nm and a fraction in range 20–90 nm. The small pores of 3–6 nm were assigned to the bulk structure of r-CeO<sub>2</sub>, whereas the pores in range 20–90 nm were assigned to the material agglomeration. The amount of small pores was nearly the same in all samples, whereas the amount of pores in range 20–90 nm markedly varied. The fraction of bulk structure pores was about 30% on samples Ni5Ce and Ni30Ce, whereas was about 15% on Ni10Ce and Ni20Ce.



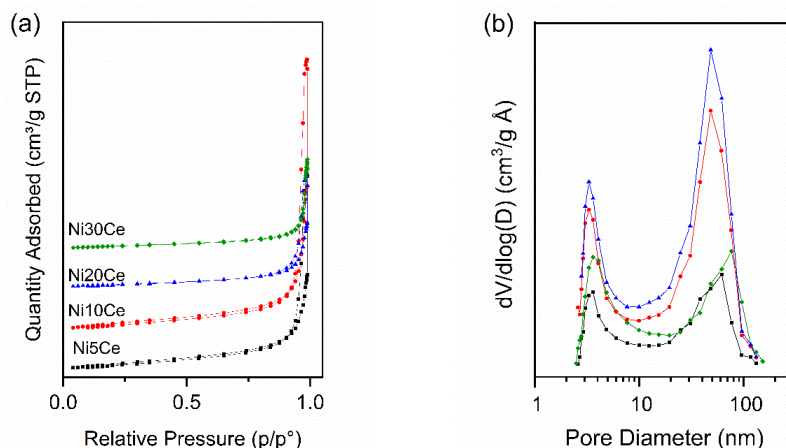


**Figure 3.** Brunauer–Emmet–Teller (BET) analysis of  $\text{Ni}_x\text{Ce}$  catalysts: (a) nitrogen adsorption and desorption isotherms as a function of  $p/p^\circ$ ; (b) PSD pore size distribution.

#### 2.4.3. Field-Emission Scanning Electron Microscopy (FE-SEM) Characterization

The FE-SEM images of the reduced catalysts with the corresponding length and width distribution histograms, related to about 100 nanorods, are reported in Figure 4. The frequency distribution histograms are plotted with bars that represent numbers of measurements within certain ranges of values, superimposed to a Gaussian curve. The average sizes are listed in Table 3. All samples showed an aspect ratio, length to width ratio, above 5 indicating a well-developed structural anisotropy characteristic of the rod-like morphology. The average length and width of the nanorods increased as the Ni content increases. In particular, the length increased from 145.9 nm of  $\text{Ni}_5\text{Ce}$  sample up to 236.1 nm of  $\text{Ni}_{30}\text{Ce}$  sample, and the corresponding width increased from 26.4 nm up to 39.6 nm. These morphological changes, related to Ni content, agree with the decrease of the specific surface area.

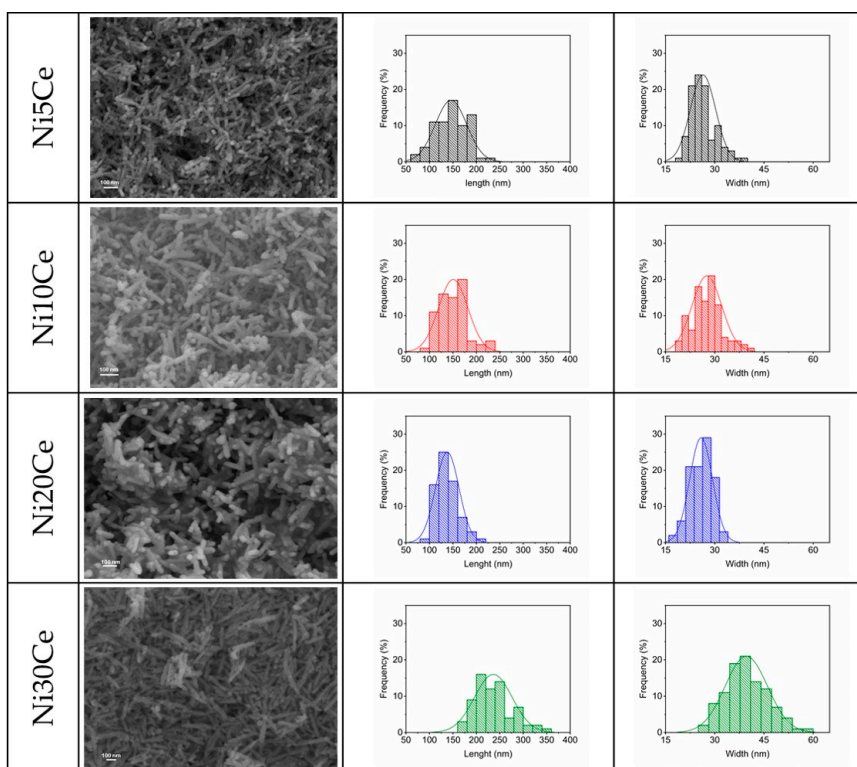


**Figure 4.** Field-emission scanning electron microscopy (FE-SEM) images of catalysts reduced at 500 °C with the corresponding length and width histogram distributions.

**Table 3.** Average values with standard deviation of length, width and aspect ratio of ceria nanorods.

	Length (nm)	Width (nm)	Aspect Ratio
Ni5Ce	145.9 ± 33.6	26.4 ± 3.9	5.5 ± 2.1
Ni10Ce	150.5 ± 31.4	27.6 ± 4.6	5.4 ± 2.1
Ni20Ce	137.8 ± 25.0	25.8 ± 3.5	5.3 ± 1.7
Ni30Ce	236.1 ± 40.2	39.6 ± 6.5	6.0 ± 1.9

### 2.5. Catalytic Activity

The catalytic activity of Ni/r-CeO<sub>2-δ</sub> catalysts for CO<sub>2</sub> methanation ( $\text{CO}_2 + 4\text{H}_2 \rightarrow \text{CH}_4 + 2\text{H}_2\text{O}$ ;  $H^\circ = -164 \text{ kJ/mol}$ ), was studied in the 200–500 °C temperature range. At higher temperature, the thermodynamic predicts a decrease of CO<sub>2</sub> conversion and the increase of produced CO, due to the reverse water-gas shift (RWGS) reaction ( $\text{CO}_2 + \text{H}_2 \rightarrow \text{CO} + \text{H}_2\text{O}$ ;  $\Delta H^0 = +38 \text{ kJ/mol}$ ). In all the catalytic tests, carbon balance was closed between ±5% and CO was the only secondary product. CO<sub>2</sub> conversion (panel a), CH<sub>4</sub> yield (panel b) and CO yield (panel c) as a function of temperature are reported in Figure 5. r-CeO<sub>2</sub> was inactive for the methanation reaction, the conversion being only 2% at 500 °C and CO being the only product. A small addition of Ni strongly increased the CO<sub>2</sub> conversion. Ni5Ce catalyst, having only 1.7 wt% of Ni, showed a remarkable activity with CO<sub>2</sub> conversion starting above 300 °C and increasing monotonically with temperature, reaching 43% at 500 °C. With increasing Ni loading, the CO<sub>2</sub> conversion curves were shifted toward lower temperature starting above 250 °C and increasing much more rapidly. Above 400 °C they began to level off and at 500 °C showed very similar conversion of about 54% due to thermodynamic limitation. At lower temperature ( $T < 400 \text{ °C}$ ), the CO<sub>2</sub> conversion increased almost linearly with the Ni loading.

The CH<sub>4</sub> yield profiles showed a characteristic volcano behavior: the CH<sub>4</sub> production increasing proportionally with the Ni loading and, at the same time, the maximum of CH<sub>4</sub> yield shifting at lower temperature with the Ni loading. Specifically, the maximum CH<sub>4</sub> yield was close to 500 °C for Ni5Ce and to 400 °C for Ni30Ce.

As explained above, the RWGS side reaction causes CO production in addition to methane. For all samples, the CO yield curves show similar onset temperature at 300 °C and increased with temperature, due to the endothermicity of RWGS [30].

Except for Ni5Ce catalyst, a close examination of the CO yield curves, reveals that the CO yield increased rapidly with temperature, showed a decreasing curve slope between 350–450 °C, and then increased again with temperature with the initial slope. In more detail, that “inflection point” in the CO yield curve occurred at 400–450 °C for Ni10Ce, and at 350–450 °C for Ni20Ce and Ni30Ce; therefore, at lower temperature by increasing Ni loading.

To further evaluate the effect of the Ni loading on the catalytic activity, the reaction was performed increasing the H<sub>2</sub>:CO<sub>2</sub> ratio from 4 to 8. By increasing the hydrogen concentration, the overall catalytic performance increased, extending the operating temperature of the catalyst at higher temperature, with a substantial decrease of unwanted CO. Figure 5d shows the variation (%) of CO<sub>2</sub> conversion, CH<sub>4</sub> and CO yields using the enriched H<sub>2</sub> mixture with respect to the stoichiometric one at 400 °C over the catalysts. The excess of hydrogen caused an increase of 40%–60% of CO<sub>2</sub> conversion and of 70%–100% of CH<sub>4</sub> yield, with a decrease of CO production up to 50%. The decrease of CO production depends on the nickel content and is larger on more concentrated samples.

The turnover frequency (TOF) for CO<sub>2</sub> conversion, obtained operating in differential conditions ( $T = 300 \text{ °C}$ , CO<sub>2</sub> conversion <10 %), increased linearly with Ni particles size as shown in Figure 6. Smaller nanoparticles appeared less active; such distinctive behavior has been reported already by other authors for Ru [21], Pd [22], Co [31] and Ni [23] supported catalysts.

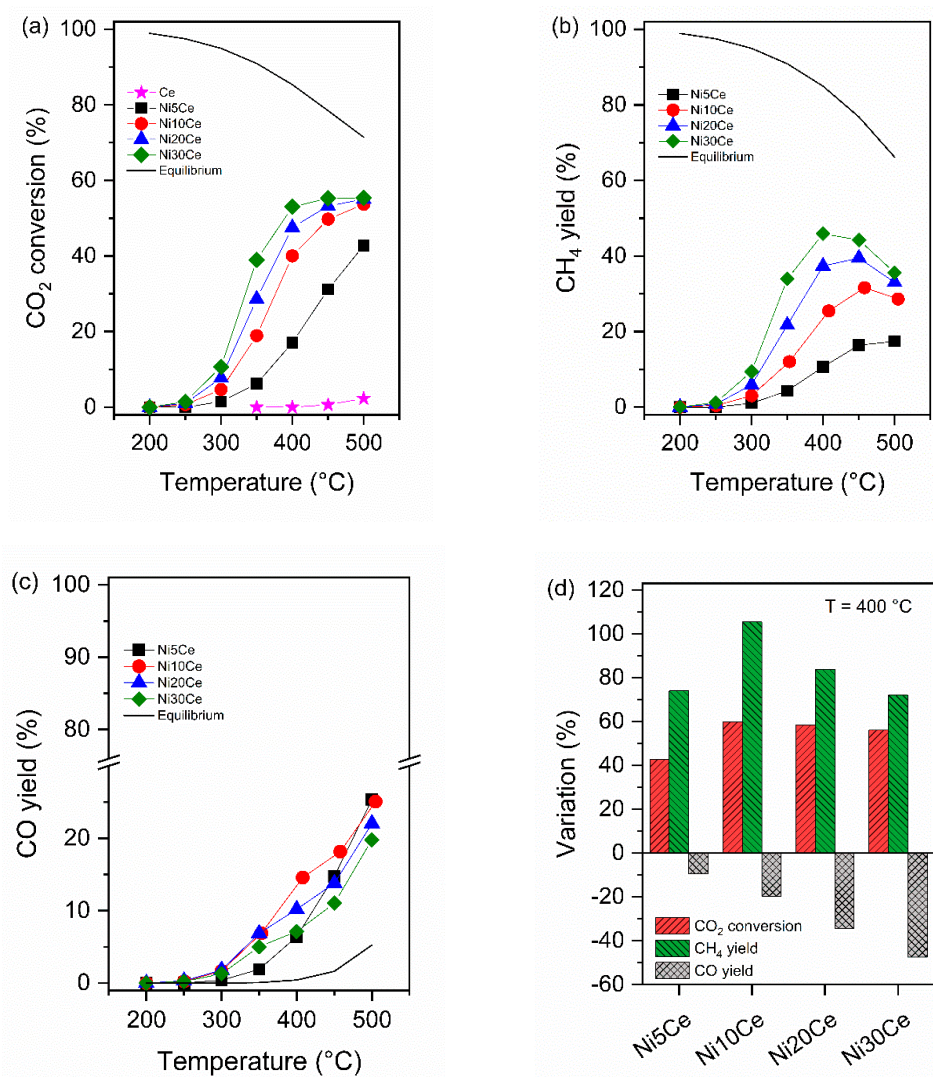


**Figure 5.** Catalytic activity: CO<sub>2</sub> conversion (a), CH<sub>4</sub> yield (b) and CO yield (c) as a function of temperature; reaction conditions: reactant mixture CO<sub>2</sub>:H<sub>2</sub>:N<sub>2</sub>:He = 1:4:2:13, catalyst mass = 40 mg, gas hourly space velocity (GHSV) = 300 L g<sup>−1</sup> h<sup>−1</sup>. Percentage variation of the CO<sub>2</sub> conversion, CH<sub>4</sub> yield and CO yield, increasing the H<sub>2</sub>/CO<sub>2</sub> ratio from 4 to 8 (d): reactant mixture CO<sub>2</sub>:H<sub>2</sub>:N<sub>2</sub>:He = 1:8:2:9, catalyst mass = 40 mg, GHSV = 300 L g<sup>−1</sup> h<sup>−1</sup>.

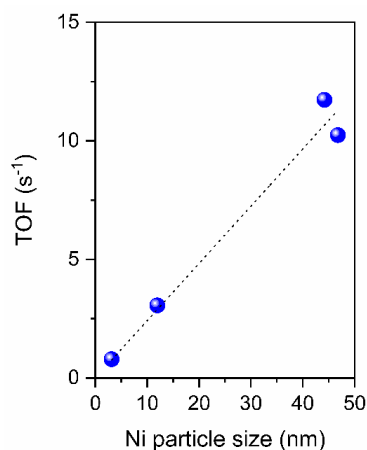


**Figure 6.** Turnover frequency of CO<sub>2</sub> conversion as a function of the average Ni particle size; reaction conditions: reactant mixture CO<sub>2</sub>:H<sub>2</sub>:N<sub>2</sub>:He = 1:4:2:13, catalyst mass = 40 mg, GHSV = 300 L g<sup>−1</sup> h<sup>−1</sup>.



A possible explanation of the observed catalytic activity is that small Ni metal nanoparticles with a greater susceptibility to oxidation [5], may have a different reaction mechanism for the CO<sub>2</sub> hydrogenation, changing the dependence of CO/CH<sub>4</sub> production on Ni particles size. CO is selectively produced on small Ni nanoparticles, whereas CH<sub>4</sub> is selectively produced on larger Ni nanoparticles.

### 3. Discussion

The on-pot hydrothermal method allows us to synthesize, with a simple procedure, catalysts with homogeneous well-developed nanorod-CeO<sub>2</sub> morphology and homogeneous nickel dispersion. As generally expected, the nickel particle size depends on nickel loading, increasing as the nickel content increases. The most diluted catalyst (1.69 wt%) has Ni particles of average diameter 3.2 nm, and eight times more concentrated catalyst (13.38 wt%) has Ni particles of average diameter 46 nm. The nickel loading causes a decrease of catalyst surface area that seems not to be influencing the catalytic activity, as the CO<sub>2</sub> conversion is linearly proportional to the Ni loading.

For the CO<sub>2</sub> methanation, two reaction mechanisms have been proposed in the literature [15]: the first involving the dissociation of CO<sub>2</sub> into CO, that is then hydrogenated into CH<sub>4</sub>, the second involving the direct hydrogenation of CO<sub>2</sub>. The first mechanism, described more in detail, may include or not the formation of formate (CHOO<sup>−</sup>) that is decomposed to CO. Anyhow, the CO intermediate is formed on the surface and then it may desorb or react with hydrogen to form CH<sub>4</sub> with a “consecutive pathway”. Some literature results over Ni/SiO<sub>2</sub> [23] indicated that the formation of m-HCOO<sup>−</sup> intermediate is an essential step in a very diluted Ni sample (0.5 wt%) and in a 10 wt% sample, but in the 10 wt% sample, formate may be also directly reduced to CH<sub>4</sub> by a “parallel pathway”. The m-HCOO<sup>−</sup> prefers the hydrogenation to CH<sub>4</sub> instead of the decomposition to CO in the presence of high H<sub>2</sub> coverage on a large Ni surface.

The CO<sub>2</sub> methanation over Ni/r-CeO<sub>2</sub>, tested in the present paper, showed two catalytic behaviors depending on nickel particle size that confirm the previously described reaction mechanism and suggest a structure-sensitivity of the CO<sub>2</sub> methanation on nickel supported on r-ceria:

- (1) The inflection point observed in the CO yield, occurs at lower temperature by increasing the Ni loading. That behavior may be explained assuming that CO is produced by a different reaction mechanism on Ni-active centers with different particle size. In agreement with the literature, we assume that on small Ni<sup>0</sup> particles, the low H<sub>2</sub> coverage, may favor the CO formation; whereas, on large Ni<sup>0</sup> particles, due to the high H<sub>2</sub> surface coverage, CO<sub>2</sub> may be directly hydrogenated to CH<sub>4</sub> therefore the rate of CH<sub>4</sub> production is higher than that of CO;
- (2) The turnover frequency for CO<sub>2</sub> conversion increases linearly with Ni particles size. Such behavior may be explained by the dependence of CO/CH<sub>4</sub> production rate on the metal particle size.

Such a scenario may be further explained by the dependence of the chemical state of a metal on its particle size. Smaller particles, interacting with the support, are partially oxidized, and therefore are catalytically active for the reverse water gas shift, producing selectively CO. Increasing the metal loading results in larger particles, with a more metallic behavior, that favor the H<sub>2</sub> chemisorption leading to pure methanation catalyst [28].

### 4. Materials and Methods

#### 4.1. Catalysts' Synthesis

Catalysts were prepared by hydrothermal one-pot method: stoichiometric amounts of cerium (III) nitrate hexahydrate and of nickel (II) nitrate hexahydrate were dissolved in 40 mL of water under stirring. The complete precipitation of salts was obtained adding drop by drop a solution NaOH 12 M up to reach pH = 8, and then stirring the slurry for 30 min. The slurry was then heated at 110 °C for 24 h in hydrothermal condition in a steel reactor with Teflon liner. The precipitated powder was filtered and washed, first with water and then with ethanol, up to neutral pH (pH = 6–7). The wet powder was dried in air and finally calcined at 500 °C for 5 h.

#### 4.2. Catalysts' Characterization

Powder X-ray diffraction was undertaken using a Philips X-Pert Pro 500 with a Cu K $\alpha$  source ( $\lambda = 1.5418 \text{ \AA}$ ) and a Bragg-Brentano  $\theta$ – $\theta$  configuration in  $10^\circ$ – $80^\circ = 2\theta$  range ( $0.05^\circ$  step size 3 s acquisition time). The crystallite sizes ( $d$ ) were estimated from the Ni (111), NiO (200) and CeO<sub>2</sub> (111) reflections by Scherrer's Equation (3):

$$d = K\lambda/(\beta\cos\theta) \quad (3)$$

The BET surface area of catalyst was measured using a Micromeritics Gemini V apparatus. Before measurement, catalysts were degassed at  $300^\circ\text{C}$  in He for 1 h. The surface area was calculated by the BET method in the pressure range  $0.05 < p/p^\circ < 0.3$ . The BET surface area S.A. was normalized by the mass fraction of nickel ( $W_{\text{Ni}}$ ) by Equation (4):

$$(S.A.)^{\text{norm}} = (S.A.)/(1 - W_{\text{Ni}}) \quad (4)$$

The pore size distribution was obtained from the desorption branch by the Barrett–Halenda (BJH) method.

H<sub>2</sub>-TPR and H<sub>2</sub>-TPD were performed by a Thermo Scientific TPDRO1100 instrument. The calcined sample was pre-treated flowing  $20 \text{ cm}^3 \text{ min}^{-1}$  of 5% O<sub>2</sub>/He gas mixture at  $500^\circ\text{C}$  for 1 h and then cooled down to  $50^\circ\text{C}$  in He. Then, 5% H<sub>2</sub>/Ar gas mixture ( $30 \text{ cm}^3 \text{ min}^{-1}$ ) was fed into the reactor and the temperature was raised to  $500^\circ\text{C}$ , with a heating rate of  $10^\circ\text{C min}^{-1}$ , holding at  $500^\circ\text{C}$  for 1 h. The sample was then cooled down to  $50^\circ\text{C}$ . H<sub>2</sub> desorption was subsequently performed flowing Ar from  $50^\circ\text{C}$  up to  $500^\circ\text{C}$  ( $30 \text{ cm}^3 \text{ min}^{-1}$ , heating rate  $20^\circ\text{C min}^{-1}$ ). The active particle size of Ni,  $d_{\text{Ni}}^{\text{TPD}}$  (nm), and the percentage of Ni dispersion,  $D_{\text{Ni}}$  (%), were calculated by Equations (5) and (6), respectively:

$$d_{\text{Ni}}^{\text{TPD}}(\text{nm}) = (10^5 f W_{\text{Ni}})/(\rho_{\text{Ni}} \eta_{\text{H}_2} N_{\text{A}} S_{\text{f}} A_{\text{Ni}}) \quad (5)$$

$$D_{\text{Ni}} (\%) = 100 \times \eta_{\text{H}_2} S_{\text{f}} M_{\text{Ni}}/W_{\text{Ni}} \quad (6)$$

$f$  = geometrical shape factor, 6 for a spherical particle

$W_{\text{Ni}}$  = Ni metal weight percentage in the sample

$\rho_{\text{Ni}}$  = density of Ni:  $8.9 \text{ g/cm}^3$

$\eta_{\text{H}_2}$  = H<sub>2</sub> desorbed in the H<sub>2</sub>-TPD experiment: mol/g of sample

$N_{\text{A}}$  =  $6.023 \times 10^{23}$

$S_{\text{f}}$  = stoichiometric factor for H<sub>2</sub> chemisorption: metal mol/gas mol = 2

$A_{\text{Ni}}$  = area occupied by Ni surface atom:  $6.51 \times 10^{-16} \text{ cm}^2$

$M_{\text{Ni}}$  = Ni atomic mass:  $58.69 \text{ g/mol}$

Nanorod morphology and chemical composition of the samples were determined by a FE-SEM (ZEISS SIGMA 300) equipped with energy dispersive spectroscopy (EDS) at 15.0 kV under a high vacuum. EDS was performed pressing sample powder at 280 MPa into pellet and analyzing and several spots with size  $10 \times 10 \text{ }\mu\text{m}^2$ . For each sample, the chemical composition was evaluated as mean value.

#### 4.3. Catalytic Activity Tests

The activity of catalysts for the methanation of CO<sub>2</sub> was measured in a quartz reactor (6 mm-diameter) operating at atmospheric pressure, connected to a flow line equipped with independent mass flow controllers. A mass of 0.040 g of catalyst, diluted with 0.100 g of silicon carbide was in situ reduced with 50% H<sub>2</sub>/N<sub>2</sub> flow ( $50 \text{ cm}^3 \text{ min}^{-1}$ ), increasing the temperature from room temperature (RT) up to  $500^\circ\text{C}$ , and isothermally kept at this temperature for 1 h. The temperature was measured by a thermocouple in contact within the catalyst bed. Reaction feed was  $10 \text{ cm}^3 \text{ min}^{-1}$  for CO<sub>2</sub>,  $40 \text{ cm}^3 \text{ min}^{-1}$  for H<sub>2</sub>,  $20 \text{ cm}^3 \text{ min}^{-1}$  N<sub>2</sub>,  $130 \text{ cm}^3 \text{ min}^{-1}$  He, total flow  $200 \text{ cm}^3 \text{ min}^{-1}$ . After catalyst

reduction, the reaction mixture feed was flowed through the reactor at 500 °C. The catalytic run was performed in temperature range −500 °C to 250 °C with decrements of 25 °C. Each temperature step was maintained for 30 min. H<sub>2</sub>O was removed from the flow before the analysis by a cold trap. The dry gas was analyzed online by a gas chromatograph (Agilent 7820) equipped with a Molecular Sieve X13 and a Haysep Q columns and a thermal conductivity detector (TCD). CO<sub>2</sub> conversion ( $X_{\text{CO}_2}$ ), CH<sub>4</sub> yield ( $Y_{\text{CH}_4}$ ) and CO yield ( $Y_{\text{CO}}$ ) were calculated using Equations (7)–(9), respectively, where %CO<sub>2</sub>, %CH<sub>4</sub> and %CO are the OUTLET gas volume concentrations:

$$X_{\text{CO}_2} = 100 \times (\% \text{CO} + \% \text{CH}_4) / (\% \text{CO}_2 + \% \text{CO} + \% \text{CH}_4) \quad (7)$$

$$Y_{\text{CH}_4} = 100 \times \% \text{CH}_4 / (\% \text{CO}_2 + \% \text{CO} + \% \text{CH}_4) \quad (8)$$

$$Y_{\text{CO}} = 100 \times \% \text{CO} / (\% \text{CO}_2 + \% \text{CO} + \% \text{CH}_4) \quad (9)$$

Carbon balance ( $C_{\text{balance}}$ ) was calculated by Equation (10):

$$C_{\text{balance}} (\%) = 100 \times F^{\text{out}} (\% \text{CO}_2 + \% \text{CO} + \% \text{CH}_4) / F^{\text{in}} \times \% \text{CO}_2^{\text{in}} \quad (10)$$

where  $F^{\text{in}}$  and  $F^{\text{out}}$  are the inlet and outlet flows respectively. Carbon balance was very close to 100% at each temperature.

The TOF for CO<sub>2</sub> conversion was calculated using the following Equation (11):

$$\text{TOF (s}^{-1}\text{)} = 10^4 F_{\text{CO}_2} X_{\text{CO}_2} M_{\text{Ni}} / (m W_{\text{Ni}} D_{\text{Ni}}) \quad (11)$$

$F_{\text{CO}_2}$  = molar flow of CO<sub>2</sub>: mol/s

$X_{\text{CO}_2}$  = conversion of CO<sub>2</sub>: %

$m$  = catalyst mass: g

## 5. Conclusions

The turnover frequency for CO<sub>2</sub> conversion increased linearly with Ni particle size. Smaller Ni nanoparticles appeared less active.

The excess of hydrogen in the reagent mixture caused an increase of 40%–60% of CO<sub>2</sub> conversion and of 70%–100% of CH<sub>4</sub> yield, with a decrease of CO production up to 50%. The selectivity to methane depended on nickel content, being larger on more concentrated samples.

The CO<sub>2</sub> methanation over nickel supported on ceria with nanorod morphology showed catalytic behaviors that can be explained by the dependence of CO/CH<sub>4</sub> selectivity on nickel particle size, suggesting a structure-sensitivity of the reaction.

**Author Contributions:** Conceptualization, S.T. and I.L.; methodology, S.T. and I.L.; investigation, E.M.; writing—original draft preparation, S.T. and I.L.; writing—review and editing, S.T. and I.L.

**Funding:** This research received no external funding.

**Conflicts of Interest:** The authors declare no conflict of interest.

## References

- De Vito, C.; Ferrini, V.; Mignardi, S.; Cagnetti, M.; Leccese, F. Progress in carbon dioxide sequestration via carbonation of aqueous saline wastes. *Periodico di Mineralogia* **2012**, *81*, 333–344. [[CrossRef](#)]
- Tuti, S.; Luisetto, I.; Leccese, F.; Kesavan, J.K.; Casciardi, S. Nickel supported on Y<sub>2</sub>O<sub>3</sub>-ZrO<sub>2</sub> as highly selective and stable CO<sub>2</sub> methanation catalyst for in-situ propellant production on Mars. In Proceedings of the 2018 5th IEEE International Workshop on Metrology for Aerospace (MetroAeroSpace), Rome, Italy, 20–22 June 2018; pp. 435–439. [[CrossRef](#)]

3. Della Pietra, M.; Santarelli, M.; Stendardo, S.; McPhail, S.; Perez-Trujillo, J.P.; Elizalde-Blancas, F. Integration of a calcium looping process (CaL) to molten carbonate fuel cells (MCFCs), as carbon concentration system: First findings. *J. CO<sub>2</sub> Util.* **2018**, *25*, 14–21. [\[CrossRef\]](#)
4. Wang, W.; Wang, S.; Ma, X.; Gong, J. Recent advances in catalytic hydrogenation of carbon dioxide. *Chem. Soc. Rev.* **2011**, *40*, 3703–3727. [\[CrossRef\]](#) [\[PubMed\]](#)
5. Kesavan, J.K.; Luisetto, I.; Tuti, S.; Meneghini, C.; Battocchio, C.; Iucci, G. Ni supported on YSZ: XAS and XPS characterization and catalytic activity for CO<sub>2</sub> methanation. *J. Mater. Sci.* **2017**, *52*, 10331–10340. [\[CrossRef\]](#)
6. Kesavan, J.K.; Luisetto, I.; Tuti, S.; Meneghini, C.; Iucci, G.; Battocchio, C.; Mobilio, S.; Casciardi, S.; Sisto, R. Nickel supported on YSZ: The effect of Ni particle size on the catalytic activity for CO<sub>2</sub> methanation. *J. CO<sub>2</sub> Util.* **2018**, *23*, 200–211. [\[CrossRef\]](#)
7. Luisetto, I.; Tuti, S.; Romano, C.; Boaro, M.; Di Bartolomeo, E. Dry reforming of methane over Ni supported on doped CeO<sub>2</sub>: New insight on the role of dopants for CO<sub>2</sub> activation. *J. CO<sub>2</sub> Util.* **2019**, *30*, 63–78. [\[CrossRef\]](#)
8. Luisetto, I.; Sarno, C.; De Felicis, D.; Basoli, F.; Battocchio, C.; Tuti, S.; Licoccia, S.; Di Bartolomeo, E. Ni supported on  $\gamma$ -Al<sub>2</sub>O<sub>3</sub> promoted by Ru for the dry reforming of methane in packed and monolithic reactors. *Fuel Process. Technol.* **2017**, *158*, 130–140. [\[CrossRef\]](#)
9. Luisetto, I.; Tuti, S.; Battocchio, C.; Lo Mastro, S.; Sodo, A. Ni/CeO<sub>2</sub>-Al<sub>2</sub>O<sub>3</sub> catalysts for the dry reforming of methane: The effect of CeAlO<sub>3</sub> content and nickel crystallite size on catalytic activity and coke resistance. *Appl. Catal. A Gen.* **2015**, *500*, 12–22. [\[CrossRef\]](#)
10. Luisetto, I.; Tuti, S.; Di Bartolomeo, E. Co and Ni supported on CeO<sub>2</sub> as selective bimetallic catalyst for dry reforming of methane. *Int. J. Hydrog. Energy* **2012**, *37*, 15992–15999. [\[CrossRef\]](#)
11. Meylan, F.D.; Moreau, V.; Erkman, S. Material constraints related to storage of future European renewable electricity surpluses with CO<sub>2</sub> methanation. *Energy Policy* **2016**, *94*, 366–376. [\[CrossRef\]](#)
12. Rönsch, S.; Schneider, J.; Matthischke, S.; Schlüter, M.; Götz, M.; Lefebvre, J.; Prabhakaran, P.; Bajohr, S. Review on methanation—From fundamentals to current projects. *Fuel* **2016**, *166*, 276–296. [\[CrossRef\]](#)
13. Frontera, P.; Macario, A.; Ferraro, M.; Antonucci, P. Supported Catalysts for CO<sub>2</sub> Methanation: A Review. *Catalysts* **2017**, *7*, 59. [\[CrossRef\]](#)
14. Aziz, M.A.A.; Jalil, A.A.; Triwahyono, S.; Ahmad, A. CO<sub>2</sub> methanation over heterogeneous catalysts: Recent progress and future prospects. *Green Chem.* **2015**, *17*, 2647–2663. [\[CrossRef\]](#)
15. Younas, M.; Loong Kong, L.; Bashir, M.J.K.; Nadeem, H.; Shehzad, A.; Sethupathi, S. Recent Advancements, Fundamental Challenges, and Opportunities in Catalytic Methanation of CO<sub>2</sub>. *Energy Fuels* **2016**, *30*, 8815–8831. [\[CrossRef\]](#)
16. Ocampo, F.; Louis, B.; Roger, A.-C. Methanation of carbon dioxide over nickel-based Ce<sub>0.72</sub>Zr<sub>0.28</sub>O<sub>2</sub> mixed oxide catalysts prepared by sol–gel method. *Appl. Catal. A* **2009**, *369*, 90–96. [\[CrossRef\]](#)
17. Iglesias, I.; Quindimil, A.; Mariño, F.; De-La-Torre, U.; González-Velasco, J.R. Zr promotion effect in CO<sub>2</sub> methanation over ceria supported nickel catalysts. *Int. J. Hydrog. Energy* **2019**, *44*, 1710–1719. [\[CrossRef\]](#)
18. Lei, Y.; Li, W.; Liu, Q.; Lin, Q.; Zheng, X.; Huang, Q.; Guan, S.; Wang, X.; Wang, C.; Li, F. Typical crystal face effects of different morphology ceria on the activity of Pd/CeO<sub>2</sub> catalysts for lean methane combustion. *Fuel* **2018**, *233*, 10–20. [\[CrossRef\]](#)
19. Du, X.; Zhang, D.; Shi, L.; Gao, R.; Zhang, J. Morphology Dependence of Catalytic Properties of Ni/CeO<sub>2</sub> Nanostructures for Carbon Dioxide Reforming of Methane. *J. Chem. Chem. C* **2012**, *116*, 10009–10016. [\[CrossRef\]](#)
20. Wang, S.; Zhao, L.; Wang, W.; Zhao, Y.; Zhang, G.; Ma, X.; Gong, J. Morphology control of ceria nanocrystals for catalytic conversion of CO<sub>2</sub> with methanol. *Nanoscale* **2013**, *5*, 5582–5588. [\[CrossRef\]](#)
21. Kwak, J.H.; Kovarik, L.; Szanyi, J. CO<sub>2</sub> Reduction on Supported Ru/Al<sub>2</sub>O<sub>3</sub> Catalysts: Cluster Size Dependence of Product Selectivity. *ACS Catal.* **2013**, *3*, 2449–2455. [\[CrossRef\]](#)
22. Kwak, J.H.; Kovarik, L.; Szanyi, J. Heterogeneous Catalysis on Atomically Dispersed Supported Metals: CO<sub>2</sub> Reduction on Multifunctional Pd Catalysts. *ACS Catal.* **2013**, *3*, 2094–2100. [\[CrossRef\]](#)
23. Wu, H.C.; Chang, Y.C.; Wu, J.H.; Lin, J.H.; Lin, I.K.; Chen, C.S. Methanation of CO<sub>2</sub> and reverse water gas shift reactions on Ni/SiO<sub>2</sub> catalysts: The influence of particle size on selectivity and reaction pathway. *Catal. Sci. Technol.* **2015**, *5*, 4154–4163. [\[CrossRef\]](#)
24. Beierlein, D.; Häussermann, D.; Pfeifer, M.; Schwarz, T.; Stöwe, K.; Traa, Y.; Klemm, E. Is the CO<sub>2</sub> methanation on highly loaded Ni-Al<sub>2</sub>O<sub>3</sub> catalysts really structure-sensitive? *Appl. Catal. B Environ.* **2019**, *247*, 200–219. [\[CrossRef\]](#)



25. Takeguchi, T.; Furukawa, S.-n.; Inoue, M. Hydrogen Spillover from NiO to the Large Surface Area CeO<sub>2</sub>–ZrO<sub>2</sub> Solid Solutions and Activity of the NiO/CeO<sub>2</sub>–ZrO<sub>2</sub> Catalysts for Partial Oxidation of Methane. *J. Catal.* **2001**, *202*, 14–24. [\[CrossRef\]](#)
26. Jalowiecki-Duhamel, L.; Zarrou, H.; D'Huysser, A. Hydrogen production at low temperature from methane on cerium and nickel based mixed oxides. *Int. J. Hydrog. Energy* **2008**, *33*, 5527–5534. [\[CrossRef\]](#)
27. Zhang, Y.; Liu, B.; Tu, B.; Dong, Y.; Cheng, M. Redox cycling of Ni–YSZ anode investigated by TPR technique. *Solid State Ion.* **2005**, *176*, 2193–2199. [\[CrossRef\]](#)
28. Perrichon, V.; Laachir, A.; Bergeret, G.; Fréty, R.; Tournayan, L.; Touret, O. Reduction of cerias with different textures by hydrogen and their reoxidation by oxygen. *J. Chem. Soc. Faraday Trans.* **1994**, *90*, 773–781. [\[CrossRef\]](#)
29. Sing, K.S.W.; Everett, D.H.; Haul, R.A.W.; Moscou, L.; Pierotti, R.A.; Rouquerol, J.; Siemieniowska, T. Reporting Physisorption Data for Gas Solid Systems with Special Reference to the Determination of Surface–Area and Porosity (Recommendations 1984). *Pure Appl. Chem.* **1985**, *57*, 603–619. [\[CrossRef\]](#)
30. Gao, J.; Wang, Y.; Ping, Y.; Hu, D.; Xu, G.; Gu, F.; Su, F. A thermodynamic analysis of methanation reactions of carbon oxides for the production of synthetic natural gas. *RSC Adv.* **2012**, *2*, 2358. [\[CrossRef\]](#)
31. Yabe, T.; Sekine, Y. Methane conversion using carbon dioxide as an oxidizing agent: A review. *Fuel Process. Technol.* **2018**, *181*, 187–198. [\[CrossRef\]](#)



© 2019 by the authors. Licensee MDPI, Basel, Switzerland. This article is an open access article distributed under the terms and conditions of the Creative Commons Attribution (CC BY) license (<http://creativecommons.org/licenses/by/4.0/>).